Chapter 3

Classical trajectory approach for tunneling

3.1 Introduction

3.1.1 The Makri-Miller model

This Chapter is concerned with an approach that accounts for tunneling by means of classical trajectories [I][1]. The approach is based on the well-known Makri-Miller model for tunneling [29]. This model is presented in the present section and related to other approaches. The classical trajectory approach is outlined in Section 3.2, followed by a numerical test in Section 3.3.

To account for tunneling processes in multidimensional trajectory based simulations, Makri and Miller [29] proposed a simple method that is based on the one-dimensional WKB result for the tunneling splitting Δ in a symmetric double-well potential [16],

$$\Delta = \frac{\hbar\omega}{\pi} \exp\left\{-\frac{1}{\hbar}\,\Theta\right\}, \tag{3.1}$$

where ω is the classical oscillation frequency of the particle in each of the wells and Θ is the classical action integral from the left turning point $-q_0$ to the right turning point $q_0 > 0$,

$$\Theta = \int_{-q_0}^{q_0} |p(q)|dq. \tag{3.2}$$

It was noted [29] that according to Eq. (3.1) one-dimensional tunneling can be interpreted in an intuitive way: a classical particle oscillates back and forth in the, say right, well; each time the turning point q_0 is encountered, there is a certain (typically small) probability $\exp\{-\Theta/\hbar\}$ for tunneling into the other well, where the rate of such events is simply proportional to the oscillation frequency

[1] paper (I) of the publication list

ω. For small tunneling probability, the cumulated tunneling probability for the time-interval 0 to t is the sum of the individual probabilities,

$$\Gamma(t) = \sum_{t_j \leq t} \exp\{-\Theta/\hbar\}, \tag{3.3}$$

where t_j are the times at which the turning point q_0 is encountered. The function $\Gamma(t)$ is a staircase function with step-size $2\pi/\omega$. Averaging over an ensemble of trajectories with different phases yields a straight line the slope of which is proportional to the tunneling splitting,

$$\Delta = 2\hbar \frac{d}{dt} \langle \Gamma(t) \rangle. \tag{3.4}$$

The equation is the basis for a generalization to the multidimensional case. To this end, it is assumed that tunneling proceeds along straight lines defined by a tunneling direction $\mathbf{d}$ (normalized, N-dimensional vector; reasonable choices are discussed below). A turning point is defined by the condition that the sign of the momentum $\mathbf{p}$ projected onto direction $\mathbf{d}$ (i.e., $\mathbf{p} \cdot \mathbf{d}$) changes from plus to minus. Each time t_j when such a classical turning point $\mathbf{q}_j^{(\mathrm{cl})}$ is encountered, the tunneling probability is computed by,

$$\Theta_j = \int_0^{\xi_{\max}} d\xi \sqrt{2[V(\mathbf{q}_j^{(\mathrm{cl})} + \xi \mathbf{d}) - V(\mathbf{q}_j^{(\mathrm{cl})})]}, \tag{3.5}$$

where $\xi_{\max}$ is the maximum length of the straight line path for which the square-root is real. The cumulated tunneling probability is then given by Eq. (3.3) with the replacement $\Theta \to \Theta_j$. The multidimensional $\Gamma(t)$ is still a staircase but with varying step-size and step-height. However, due to the exponential factor only the smallest Θ_j contribute to the sum. The tunneling splitting is given - in complete analogy to the 1D case - by Eq. (3.4). The ensemble of trajectories is the invariant torus corresponding to a certain eigenstate, i.e., a numerical implementation may use adiabatic switching or normal mode sampling [99] (cf. Section 2.1.5). The quasi-periodicity of the dynamics on the invariant torus ensures $\Gamma(t)$ to be linear also in the multidimensional case. However, when the initial condition are generated by an approximate method like normal mode sampling, the sampling error leads to deviations from linearity [99].

For a multidimensional system the choice of the tunneling direction $\mathbf{d}$ is non-unique. In the original paper, Makri and Miller proposed to use the shortest straight-line connection between the caustics of the left and right invariant tori. Their original proposal is illustrated in Fig. 3.1 for the SMC and ASMC case. For the SMC case the tunneling direction *always* coincides with the large amplitude coordinate . For the ASMC case does the tunneling direction not only depend on

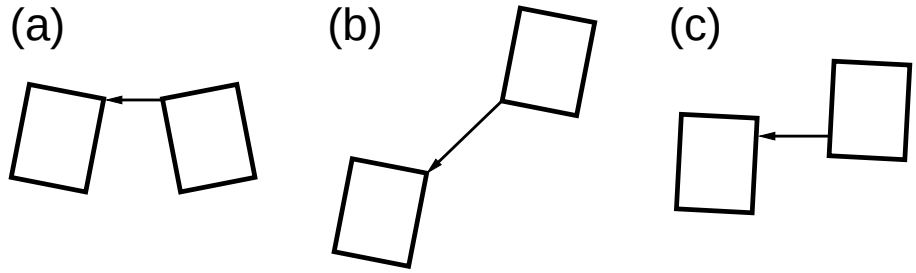

Figure 3.1: Tunneling directions as proposed by Makri and Miller [29]. Tunneling is assumed to occur along straight lines parallel to the given arrows. Thick black lines correspond to caustics of invariant tori. (a) SMC case, (b) ASMC with large displacement, and (c) ASMC with small displacement.

the coupling strength, but also on the eigenstate of interest. Alternative choices were discussed in the literature [100, 99, 101, 102].

It was shown that the Makri-Miller model can be used to determine (or estimate, at least) tunneling splittings for multidimensional systems. For instance, full-dimensional calculations using realistic PES [43] or on-the-fly molecular dynamics [103] were carried out. Moreover, it was shown that the model can be used to incorporate tunneling into classical trajectory simulations [102]. To this end, a particle that hits a turning point was physically displaced along the straight line tunneling direction with probability equal to $\exp\{-\Theta/\hbar\}$.

3.1.2 Tunneling models based on multidimensional Wentzel-Kramers-Brillouin theory

Takada and Nakamura [30] showed that there are two extreme cases of tunneling in a SMC potential: (a) tunneling proceeds through the C region or (b) tunneling proceeds through the I region. Case (a) and (b) correspond to small and large coupling, respectively. The situation is sketched in Fig. 3.2. In case (a) the saddle point falls into the C region. No trajectories can be defi ned in that region and the action function is complex; especially, it is complex along the symmetry line. Interestingly, in case (a) the MM is expected to perform best, because in the limit case of vanishing coupling, the starting equation [Eq. (3.1)] of the MM is the exact semiclassical result. On the opposite, in case (b) the MM is expected to perform poorly, because there is a large effective barrier for all straight line paths.

In the I region the semiclassical wave function can be expressed as

$$\Psi(x,q) = \exp\left\{-\frac{1}{\hbar}S_I(x,q) - \tilde{S}(x,q)\right\}, \tag{3.6}$$

where $S_0 \equiv i\,S_I$ and $S_1 \equiv -\tilde{S}$ [cf. Eq. (2.13)] satisfy the HJE [Eq. (2.15)]

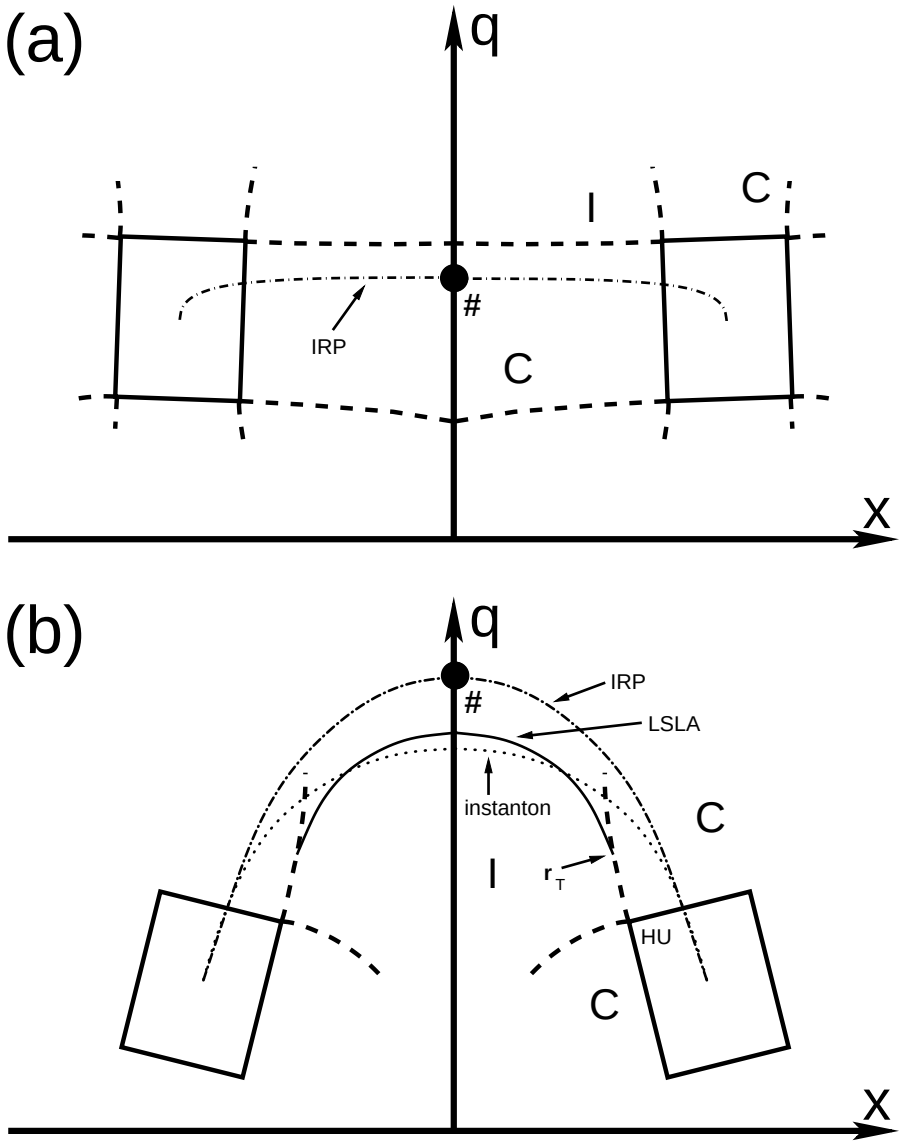

Figure 3.2: Tunneling mechanisms (schematic) for the SMC-PES. The saddle point (∓) and the IRP (dash-dotted) is indicated. Thick solid and dashed lines correspond to caustics of the allowed and forbidden regions, respectively. (a) small coupling, and (b) intermediate coupling. The instanton (dotted) trajectory is indicated. The LSLA trajectory (thin solid) starts from the take-off point $\mathbf{r}_T$ on an $C-I$-caustic.

and transport equation [Eq. (2.16)], respectively. Especially, S_I satisfies the HJE for the upside-down PES, $E - V(\mathbf{r})$ and $\mathbf{p}(\mathbf{r}) = \boldsymbol{\nabla} S_I(\mathbf{r})$ is the momentum of a classical trajectory on the upside-down PES traversing position $\mathbf{r}$. Here, vectors $\mathbf{r}$ denote a position in the 2D space (x, q).

It is assumed that there is a single point $\mathbf{r}_s = (0, q_s)$ on the symmetry line Σ where the exponent is stationary,

$$\left.\frac{\partial S_I(x,q)}{\partial q}\right|_{\mathbf{r}_s} = 0, \tag{3.7}$$

i.e., there is a particular trajectory with momentum perpendicular to the symmetry line at $\mathbf{r}_s$. [If more than one trajectory satisfies Eq. (3.7) then only the one with smallest action contributes.] In the vicinity of $\mathbf{r}_s$ on Σ, the action S_I can be expanded into a second-order Taylor series with respect to q, $S_I(x = 0, q) \approx S_I(0, q_s) + 0.5\, S_I''(0, q_s)\, (q - q_s)^2$, where S_I'' is the second derivative with respect to q. The tunneling splitting can be determined by inserting Eq. (3.6) into Herring's formula for the SMC case [Eq. (2.62)], evaluating the derivative with respect to x, inserting the truncated Taylor expansion for Ψ, and performing the Gaussian integral analytically in the semiclassical limit $\hbar \to 0$ [30],

$$\Delta = B\, \exp\{-2S_I(0, q_s)/\hbar\}, \tag{3.8}$$

with the prefactor

$$B = \hbar \sqrt{\frac{\pi\hbar}{S_I''(0, q_s)}}\, e^{-2\tilde{S}(0,q_s)}\, 2|p_x(0, q_s)|, \tag{3.9}$$

where $p_x = \partial S_I/\partial x$ is the momentum in x-direction. Thus, in this approach, the tunneling splitting is dominated by a particular trajectory. This trajectory is defined by the condition Eq. (3.7) and the boundary conditions of the field of trajectories corresponding to the I region. This boundary conditions were discussed in Section 2.1.3.

When the energy is kept in the HJE (2.15) [as opposed to Eq. (2.23)] then there are R, C, and I regions around each HU point. The equi-amplitude lines of the I region smoothly connect to the equi-amplitude lines of the C regions, i.e., the particular trajectory tangentially approaches a caustic of a C region at the so-called *take-off* point $\mathbf{r}_T$. The situation is depicted in Fig. 3.2b. The trajectory is suggestive of a tunneling path, but the trajectory connects to the C region and the c-valued S of the C region does not define a field of trajectories, i.e., the path is undefined there.

Takada and Nakamura [30] derived analytical expressions for the tunneling splitting by making simplifying assumptions: Separability and linearity of the

PES in between the HU point (cf. Fig. 3.2) and the take-off point $\mathbf{r}_T$. Then, the tunneling splitting according to this *locally separable linear approximation* (LSLA) is given by Eq. (3.8), where $S_I(0, q_s) = S_{\mathrm{LSLA}}$ is the action along the path, HU point $\rightarrow$ take-off point $\rightarrow$ $(0, q_s)$. The derivation of the prefactor is straightforward [30]. The LSLA can be applied for ground and excited states as long as the invariant torus exists. An application to multidimensional systems with $N > 2$ seems not to be feasible because it involves a search for the take-off point in multidimensional space.

Under the assumption that the harmonic approximation is valid for the wavefunction in the allowed region one can extend the I region to the minima such that R and C regions vanish (cf. Section 2.1.3). The PES is inverted, $-V(x, q)$, and the minima become hills. Consider the right minimum: a field of trajectories that emanate from the right minimum in the infinite past can be defined [58]. Only an extreme tunneling trajectory is considered, that satisfies Eq. (3.7) at certain point q_s (that may be different from the LSLA result). Such trajectory starts-off from the symmetry line with momentum perpendicular to the symmetry line and approaches the hill along the weakest mode [58]. Benderskii *et al.* [58] found a splitting formula similar to Eq. (3.8), where $S_I \equiv S_{\mathrm{inst}}$ is the action along half of the extreme tunneling trajectory. The extreme tunneling trajectory is called the *instanton*. This name derives from a related method that determines the ground state tunneling splitting from the semiclassical approximation to the partition function [8, 87]. The *instanton theory* was also generalized to treat low vibrationally excited states [58, 104, 105].

Recently, Mil'nikov and Nakamura [59] gave an implementation of the instanton theory that is applicable to multidimensional systems. The performance of the new method was demonstrated, e.g., for malonaldehyde [106] and the formic acid dimer [107]. A related approximate approach was introduced by Tautermann *et al.* [108] (see below).

3.1.3 Other tunneling models

Tunneling paths are also discussed in the context of generalized transition state (TST) theories [73, 67, 109]. Usually adiabatic separability of the intrinsic reaction coordinate s and the remaining DOF $\mathbf{q}$ is assumed, where $(s, \mathbf{q})$ form a curvilinear coordinate system. It was shown that the effect of small IRP curvature can be accounted for by an effective s-dependent mass $\mu_{\mathrm{eff}}(s)$ [110] in the adiabatic Hamiltonian,

$$H(p_s, s) = \frac{1}{2\mu_{\mathrm{eff}}(s)} p_s^2 + V_1(s) + E_0(s), \tag{3.10}$$

where p_s is the momentum conjugated to s and $E_0(s)$ is the zero-point energy (ZPE) of the $\mathbf{q}$-modes. (A full-dimensional reaction path Hamiltonian with exact kinetic energy and harmonic approximation with respect to the DOF orthogonal to the reaction path was derived by Miller *et al.* [111].) Recall, s coincides at the minimum with the weakest mode that is symmetrically available. The exponent of the tunneling probability is given by an integral analogous to Eq. (3.2) between the two inner turning points $\pm s_0$ on the IRP at energy E. The method was termed the *small curvature tunneling approximation* (SCT). (A derivation of a formal condition for this approximation to be valid can be found in Ref. [110].) Undoing the introduction of the effective mass leads to tunneling paths that lie on the concave side of the IRP and cross the symmetry surface at a position displaced from the saddle point. This effect was already investigated by Marcus and Coltrin [112] and it was termed *corner cutting*. The same effect can be found for the instanton and LSLA paths (cf. Section 3.1.2).

For large IRP curvature the SCT breaks down and straight-line paths are favored leading to the *large curvature tunneling approximation* (LCT) (or *sudden approximation*). The straight-line paths go from one turning point on one side of the IRP to the other side, i.e., they cross a non-adiabatic region, the so-called *reaction swath*. However, already Marcus and Coltrin [112] pointed out that the "true" tunneling path should satisfy the least action (or Hamilton's) principle of classical mechanics (cf. Appendix A.1). The formal justification for such a principle is given by the multidimensional WKB theory (cf. Section 3.1.2): the solution of the HJE in the I region is given by classical trajectories propagated on the inverted PES. (Classical trajectories satisfy Hamilton's principle by definition.)

Garrett and Truhlar (GT) [113] proposed to consider a family of paths parameterized by a parameter α ($0 \leq \alpha \leq 1$). If the case of two equivalent minima is assumed, then the two turning points on the IRP can be denoted as $\pm s_0$. The GT paths are defined by

$$\begin{aligned}\tilde{\mathbf{X}}(s;\alpha) &= (1-\alpha)\mathbf{X}(s) \\ &+ \quad \alpha\left[\mathbf{X}(+s_0) + (s-s_0)(\mathbf{X}(+s_0) - \mathbf{X}(-s_0))/2s_0\right], \end{aligned} \tag{3.11}$$

where $\mathbf{X}(s)$ is the coordinate representation of the IRP [cf. Eq. (2.49)]. For $\alpha = 0$ the GT path coincides with the IRP and corresponds to the the tunneling path in the small-curvature limit; for $\alpha = 1$ the GT path is a straight line connecting the two turning points and corresponds to the large-curvature limit. Recently, Tautermann *et al.* [108] implemented such an approach numerically and determined tunneling splittings. (The available computer power was insufficient in 1983, so GT had to resort to further approximations.) The approach was checked against a fully optimized tunneling path for the malonaldehyde molecule and it was concluded

that the optimized GT path is a reasonable approximation. Note, in contrast to the statement in Ref. [114], the family of GT paths covers a curved but *two-dimensional* submanifold of the full-dimensional confi guration space only.

3.2 The extended Makri-Miller model (EMM)

3.2.1 Motivation

In Section 3.1.2 it was noted that the straight-line approximation of the Makri-Miller model may break down in a situation sketched in Fig. 3.2b. For any set of fi xed SMC parameters a, $\tilde{c}$, λ, and Ω such a situation is met for large enough λ, since the minima are at $(\pm\sqrt{a/\tilde{c}}, -\lambda a/\tilde{c}\Omega^2)$ and the saddle point is at $(0,0)$. (However, for λ too large, all invariant tori are destroyed.) The break-down of the straight-line approximation motivates the use of the tunneling trajectories of the TU theory [27, 60, 28] (cf. Section 2.1.4), because - unlike straight-lines - these *TU trajectories* are related to approximate solutions of the multidimensional HJE [cf. Eq. (2.20)]. Therefore, the objective of this Section is the derivation of an extended Makri-Miller model (EMM) that accounts for tunneling by means of TU trajectories. The new method is numerically tested in Section 3.3 and applied to generic SMC-PES, model PES of the carboxylic acid dimer, and the HO_2^- anion. It is shown that the new model can also account for tunneling through the I region as depicted in Fig. 3.2b. In particular, two questions are addressed:

(Q1) For which situations are the generalizations effective and lead to a signifi - cant improvement of the results?

(Q2) Can vibrationally excited states be treated with the new method?

Q2 is of special importance in view of the the new developments concerning the instanton theory [59, 106, 105, 107], which can treat tunneling splittings of ground and singly excited states only.

The discussion primarily addresses the SMC case, because only in this case a pronounced mode-selectivity (spanning orders of magnitude) can be anticipated. The ASMC case is complicated by the dependence of the tunneling splitting upon the phase of the wave function along the symmetry line (cf. Section 2.2.3). The squeezed (SQZ) case is not interesting for the present purpose, because straight line paths are well suited, especially the instanton is a straight line in this case.

3.2.2 Turning points and caustics

In a one-dimensional system turning points q_0 are uniquely defi ned by the energy E and PES $V(q)$ via condition $V(q_0) = E$. In a multidimensional system classi-

cally allowed and classically forbidden regions of configuration space are divided by caustics. A caustic is a surface (or line in 2D) of points at which trajectories cross from one branch of the momentum function to a neighboring branch (cf. Section 2.1.3), i.e., a caustic is a property of an ensemble of neighboring trajectories. This ensemble is mathematically described by the Lagrange manifold (e.g., invariant torus) on which the branches of the momentum function are defined. *For non-separable potentials one cannot uniquely define the kinetic energy for a particular coordinate, thus it is impossible to obtain the turning points* [115].

Therefore, the following practical approximate definition for multidimensional turning points is considered. Let $\mathbf{d}_j$ be the N normal mode vectors corresponding to the right minimum of a double-well system. For a harmonic system, turning points are given by the condition

$$\mathbf{d}_j \cdot \mathbf{p} = 0, \tag{3.12}$$

where $\mathbf{p}$ is the momentum vector. This condition is also reasonable for the modestly anharmonic case (for instance, cf. Fig. 3.4).

3.2.3 Computational algorithm

The algorithm of the extended Makri-Miller model involves the following steps [I]:

1. Initial conditions for an ensemble of trajectories according to the multidimensional quantization rule [Eq. (2.36)] are selected either by adiabatic switching or by normal mode sampling (cf. Section 2.1.5). All the trajectories are initially located either in the right or left well.

2. A trajectory of the ensemble is propagated in the R region for a certain amount of time T. During this time the trajectory will hit classical turning points $\mathbf{q}_n^{(\mathrm{cl})}$. These turning points are determined by the condition $\mathbf{d}_j \cdot \mathbf{p}_t = 0$ [Eq. (3.12)].

3. Each time the trajectory hits a classical turning point $\mathbf{q}_n^{(\mathrm{cl})}$, the parity σ_j of the corresponding direction $\mathbf{d}_j$ is flipped from +1 to -1. The trajectory is then propagated in the forbidden region according to the equations of motion (2.30-2.31).

4. The condition Eq. (3.12) is also used to determine *non-classical* turning points outside the R-region: When the turning point condition is fulfilled for a trajectory in the forbidden region then another parity σ_k of the corresponding direction is flipped from +1 to -1. Both trajectories in the forbidden region, the one with $\sigma_j = -1$ and $\sigma_k = +1$ as well as the one with

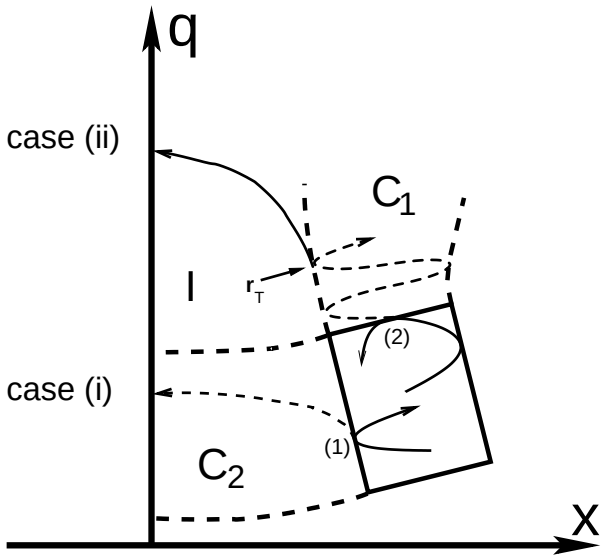

Figure 3.3: Right well of Fig. 3.2 for an unspecified saddle point. Tunneling trajectories emanating from two classical turning points, (1) and (2), are shown. Case (i) and (ii) correspond to tunneling through the C and I region, respectively.

$\sigma_j = -1$ and $\sigma_k = -1$, will be integrated in this case. And so on for more than two dimensions.

5. When a trajectory, that is propagated in the forbidden region, crosses the symmetry line Σ, the complex action W_n of that trajectory is computed. The action W_n is given by the integral Eq. (2.35) along the trajectory from $\mathbf{q}_n^{(\mathrm{cl})}$ to the crossing point on the symmetry line. There may be several trajectories that emanate from one classical turning point $\mathbf{q}_n^{(\mathrm{cl})}$. Only that action W_n is kept, that has the smallest imaginary part.

6. The contributions of all non-classical trajectories with smallest action that have emanated from classical turning points $\mathbf{q}_n^{(\mathrm{cl})}$ at time t_n are summed up according to:
$$\Gamma(t) = \sum_{t_n \leq t} \exp\left\{-\frac{2}{\hbar}|\mathrm{Im}\, W_n|\right\}. \tag{3.13}$$
If the initial conditions correspond to an invariant torus then the ensemble average, $\langle\Gamma(t)\rangle$, is a straight line. The tunneling splitting is given by [cf. also Eq. (3.4)]:
$$\Delta = 2\hbar\frac{d}{dt}\langle\Gamma(t)\rangle. \tag{3.14}$$

For the case of a SMC PES the algorithm is illustrated in Fig. 3.3. Vectors of the 2D space (x, q) are denoted as $\mathbf{r}$. One may distinguish two important cases: In case (i) a classical trajectory (solid) propagated in the R-region hits a turning

point $\mathbf{r}^{(\mathrm{cl})}$ "(1)" at the C_2-R caustic. The emanating TU trajectory (dashed) resides solely in the C_2 region and hits the symmetry line. In case (ii) a turning point "(2)" of the C_1-R caustic is touched giving rise to a TU trajectory in the C_1 region. This trajectory hits several non-classical turning points at the caustics of the C_1 and neighboring I regions. For instance, the third non-classical turning point $\mathbf{r}_T$ of that trajectory is located at the $I - C_1$ caustic. A second parity is flipped at that point giving rise to an additional TU trajectory that is propagated in the I region. This trajectory then crosses the symmetry line. By this procedure, many TU trajectories are generated for a single classical turning point $\mathbf{r}^{(\mathrm{cl})}$ and several of them will cross the symmetry line. Only the TU trajectory with smallest imaginary action is kept, the contributions of the other trajectories are discarded. This is motivated by the least action principle.

In the case of small γ, when the saddle point falls into the C_2 region, the TU trajectories in that region are expected to have smaller action than those that propagate through the C_1 and I region. And vice-versa for the case of larger γ, when the saddle point falls into the I region. The situation in this case is reminiscent of the LSLA approximation. Therefore one may call the second non-classical turning point $\mathbf{r}_T$ of the shown trajectory the *take-off* point. Compared to the LSLA there are two important differences: (i) TU theory assumes separability in the C_1 region, and (ii) the C_1-I boundary is determined by the turning point condition Eq. (3.12), i.e., the turning point condition is used for the classical forbidden *and* allowed region. For the LSLA approximation the C_1-I boundary was approximated by a straight line continuation of the *exact* C_2-R boundary. The two approximations, (i) and (ii), need to be justified by numerical tests.

3.3 Numerical test of the extended Makri-Miller model

3.3.1 Generic symmetric mode coupling potentials

The SMC Hamiltonian is given by Eq. (2.61). There are four parameters, a, c, Ω, and λ. The set of parameters can be reduced without restrictions by introducing dimensionless positions $(\tilde{x}, \tilde{q})$ by

$$x = x_m \tilde{x}, \tag{3.15}$$

$$q = x_m \tilde{q}, \tag{3.16}$$

where $x_m = \sqrt{a/\tilde{c}}$ is the minimum position of x, and by dividing the SMC Hamiltonian by $8\,\Delta E_{\fdownarrow} = 2a^2/\tilde{c}$. The new SMC Hamiltonian $\tilde{H}_{\mathrm{SMC}}$ reads

$$\begin{aligned}\tilde{H}_{\mathrm{SMC}} = & -\frac{g^2}{2}\left(\frac{\partial^2}{\partial\tilde{x}^2}+\frac{\partial^2}{\partial\tilde{q}^2}\right) \\ & + \frac{1}{8}(\tilde{x}+1)^2(\tilde{x}-1)^2+\frac{\omega^2}{2}\left[\tilde{q}+\frac{\gamma}{\omega^2}(\tilde{x}^2-1)\right]^2, \end{aligned} \tag{3.17}$$

where the constant $1/8$ is added and the oscillator DOF is shifted by γ/ω^2. The new parameters are defined by

$$g = \hbar\tilde{c}/a\sqrt{2a} = \hbar\Omega_x/8\Delta E_{\fdownarrow} \tag{3.18}$$

$$\omega = \Omega/\sqrt{2a} = \Omega/\Omega_x, \tag{3.19}$$

$$\gamma = \lambda/2\sqrt{a\tilde{c}}, \tag{3.20}$$

where $\Omega_x = \sqrt{2a}$ is the harmonic frequency corresponding to the minima of the original SMC Hamiltonian. The new Hamiltonian is used throughout this work and was first introduced by Takada and Nakamura [30]. It depends on three parameters only. Formally, the parameter g corresponds to the reduced Planck constant of the new SMC Hamiltonian. Moreover, it is related to the dimensionless mass m by $m = g^{-1/2}$ where $\hbar = 1$. The remaining parameters, ω and γ, have the same meaning as the original Ω and λ, respectively. The harmonic approximation for the one-dimensional double-well part (x direction) of the PES of Eq. (3.17) at the minima yields a dimensionless force constant of $\omega_x^2 = 1$. Thus, ω^2 is the ratio of the minimum force constant of the one-dimensional double well and the force constant of the displaced harmonic oscillator. The oscillation frequency of a harmonic oscillator with mass $1/g^2$ and force constant 1 is $\omega^* = g$. The period $T^* = 2\pi/g$ (dimensionless time) defines a characteristic time scale. Subsequently, the tilde is dropped, $(\tilde{x},\tilde{q}) \to (x,q)$, to simplify the notation.

An actual parameter set will be reported in the form (ω,γ,g). For each parameter set an ensemble of 100 trajectories was propagated to determine the tunneling splitting $\Delta_{\mathbf{n}}$, where $\mathbf{n} = (n_x, n_q)$; the quantum numbers n_x and n_q correspond approximately to the DOF x and q, respectively. Each trajectory was propagated for 125-250 $\times\ T^*$. The numerical integration of the equation's of motion were performed using a symplectic trajectory integrator of fifth order [116] with a fixed step size of typically $10^{-3}\,T^*$. The adiabatic switching method (cf. Sec. 2.1.5) was used to determine the initial conditions corresponding to the set of quantum numbers $\mathbf{n}$. Fig. 3.4 shows turning points obtained by the turning point condition [cf. Eq. (3.12)] for the parameter set $(0.9, 0.7, 0.04)$; the projection of the torus unveils a moderate distortion with respect to the rectangular shape. The approximate turning point condition leads to a slight disagreement between turning

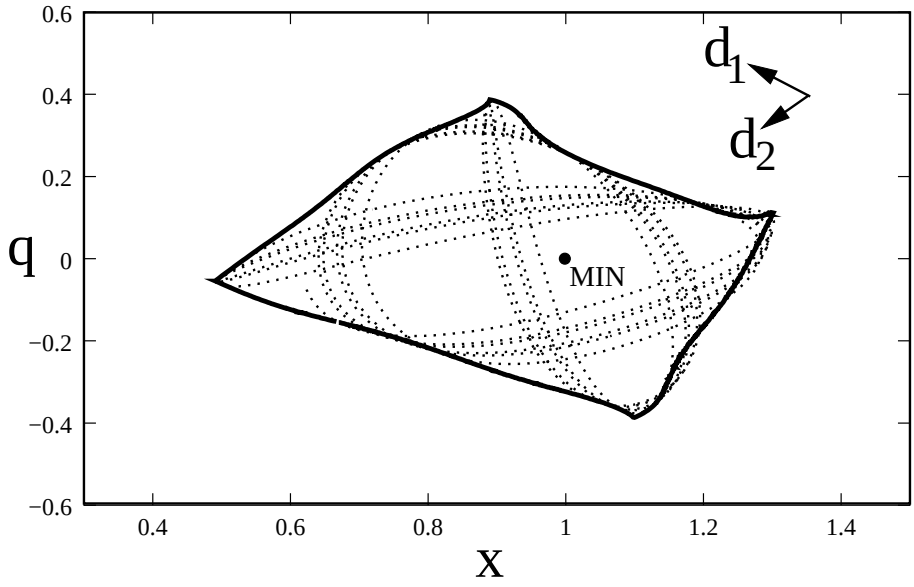

Figure 3.4: Approximate turning points of the ground state ensemble of the SMC Hamiltonian [Eq. (3.17)] with dimensionless parameters $(\omega, \gamma, g) = (0.9, 0.7, 0.04)$. The turning points are generated by the condition Eq. (3.12) and are connected by a thick black line. A fraction of an individual trajectory inside the R-region is also shown (dashed). The approximate turning point condition leads to a slight disagreement between turning points and exact caustics of the invariant torus corresponding to the ensemble of trajectories.

	$\Delta_{(0,0)}$ (ground state)				
(ω, γ)	QM[(a)]	MM	EMM	inst[(a)]	LSLA[(a)]
$(0.5, 0.25)$	5.73(-9)	2.31(-9)	6.80(-9)	6.4(-9)	5.8(-9)
$(0.5, 0.125)$	1.65(-8)	2.23(-8)	2.44(-8)	1.9(-8)	1.5(-8)
$(0.8, 0.64)$	4.55(-9)	8.71(-11)	5.12(-9)	5.2(-9)	6.8(-9)
$(0.8, 0.32)$	1.49(-8)	7.30(-9)	1.03(-8)	1.7(-8)	1.6(-8)
$(0.8, 0.16)$	2.15(-8)	5.78(-8)	2.82(-8)	2.5(-8)	2.1(-8)
$(1.5, 1.125)$	1.75(-8)	4.37(-11)	3.74(-8)	2.0(-8)	2.9(-8)
$(0.6, 0.2)$[(b)]	1.19(-4)	1.61(-4)	1.90(-4)	1.46(-4)	1.16(-4)

[(a)] Ref. [30]

[(b)] $g = 0.08$

Table 3.1: Ground state tunneling splitting ($\Delta_{(0,0)}$) for the SMC Hamiltonian Eq. (3.17). Results for the EMM are compared with quantum (QM), MM, LSLA, and instanton theory (inst) results (cf. list of acronyms). The parameters correspond to the case sketched in Fig. 3.2b. Except for the last row, the parameter g is 0.04. Values are reported as $A(-B)$ which means $A \cdot 10^{-B}$.

points and exact caustics of the invariant torus corresponding to the ensemble of trajectories. Other parameter sets discussed in the present Section correspond to a less pronounced distortion, i.e., the turning point conditions is appropriate.

The case of intermediate coupling is considered first (cf. Fig. 3.2b). Table 3.1 shows tunneling splitting obtained by the present EMM and various alternative methods. The instanton theory and the LSLA were briefly reviewed in Section 3.1.2. The numerical exact quantum mechanical (QM) results were obtained by a direct diagonalization of the Hamiltonian on a grid. These results as well as the semiclassical results for the instanton theory and LSLA are taken from Ref. [30] where the computational details can also be found. The MM results were obtained within this work; the sampling parameters were the same as for the EMM.

The saddle point is given by $\mathbf{r}_{\mathrm{SP}} = (0, \gamma/\omega^2)$. Therefore, at fixed values of ω, the tunneling splitting increases for decreasing γ. This can be seen in the first and second ($\omega = 0.5$) and in the third to fifth column ($\Omega = 0.8$), respectively. The results obtained for the instanton theory as well as for the LSLA agree reasonably well with the QM results; the order of magnitude is correctly reproduced for all parameter sets shown in Table 3.1. The deviations of the instanton results are between +12% and +23%; the LSLA deviates between -10% and +66% from the QM results. The results obtained with the EMM are also reasonable with maximum deviation +114% for $(1.5, 1.125, 0.04)$. Other deviations are between -30% and +60%. Nevertheless, even for the worst deviation the order of magnitude

of the splittings is reasonably reproduced. This has to be contrasted to the MM results. While results for several parameters are reasonable as well, there are parameter sets for which the deviation is few orders of magnitude. For instance, the splitting obtained with parameter set $(1.5, 1.125, 0.04)$ is about three orders of magnitude too small. For the parameter set $(0.8, 0.64, 0.04)$ the tunneling splitting is about 2 orders of magnitude too small.

For each action W_n that is computed for a classical turning point $\mathbf{r}_n^{(\mathrm{cl})}$ there is a unique point $\mathbf{r}_n^{(\Sigma)}$ on the symmetry line (or surface, in more than 3 dimensions) Σ. For the MM $\mathbf{r}_n^{(\Sigma)}$ is determined by a straight line starting from $\mathbf{r}_n^{(\mathrm{cl})}$, and for the EMM $\mathbf{r}_n^{(\Sigma)}$ is the point at which a trajectory in the forbidden region crosses Σ. According to Section 2.2 $\exp\{-2\,W_n/\hbar\}$ is the exponential part of a semiclassical wavefunction at $\mathbf{r}_n^{(\Sigma)}$. In Fig. 3.5 scatter plots of the tunnel probability

$$P_{\mathrm{tunnel}}(q) = \exp\{-2\,W_n/\hbar\} \tag{3.21}$$

vs. position on the symmetry line q (where $x = 0$ on Σ) for the semiclassical methods, EMM and MM, are compared with the density $|\Psi(0,q)|^2$ of the QM symmetric ground state along the symmetry line. The maxima of the EMM and QM data are normalized to one, i.e., the pre-exponential factor is assumed to vary only slowly along q compared to the exponential part. The data of the MM is normalized by the normalization constant obtained for the EMM. This is justified, because both methods only yield the exponential part of the wavefunction. The SMC parameters are $g = 0.04$ and $\Omega = 0.64$; results for three values of γ are shown.

In the upper panel ($\gamma = 0.16$) the saddle point is located at $q = 0.25$. Due to corner cutting (cf. Section 3.1.3) the maximum of $|\Psi|^2$ at $q = 0.16$ does not coincide with the saddle point where the energy is lowest along the symmetry line. The scatter plot of the EMM appears to be shifted systematically by about 0.025 to the right; despite this small shift, for $q > 0$ it agrees quite well with the numerically exact results. For $q < 0$ there are two branches of the scatter plot. This can be attributed, respectively, to trajectories that tunnel from the C_2 into the I region and to trajectories that tunnel from the C_1 into the I region. Two approximation contribute to this observation: (i) the turning point condition yields only approximate caustics in the forbidden (and allowed) regions, and (ii) the TU theory assumes separability in the C regions. The scatter plot of the MM shows a single branch that rises to about the maximum of the QM curve. Note that MM and EMM are normalized by the same constant. The maximum of the MM data is only about 4% lower than the maximum of the EMM data, but the MM sampling deviates strongly from the QM results. This is not surprising, because there are no trajectories in the I region. However, for the tunneling splittings only

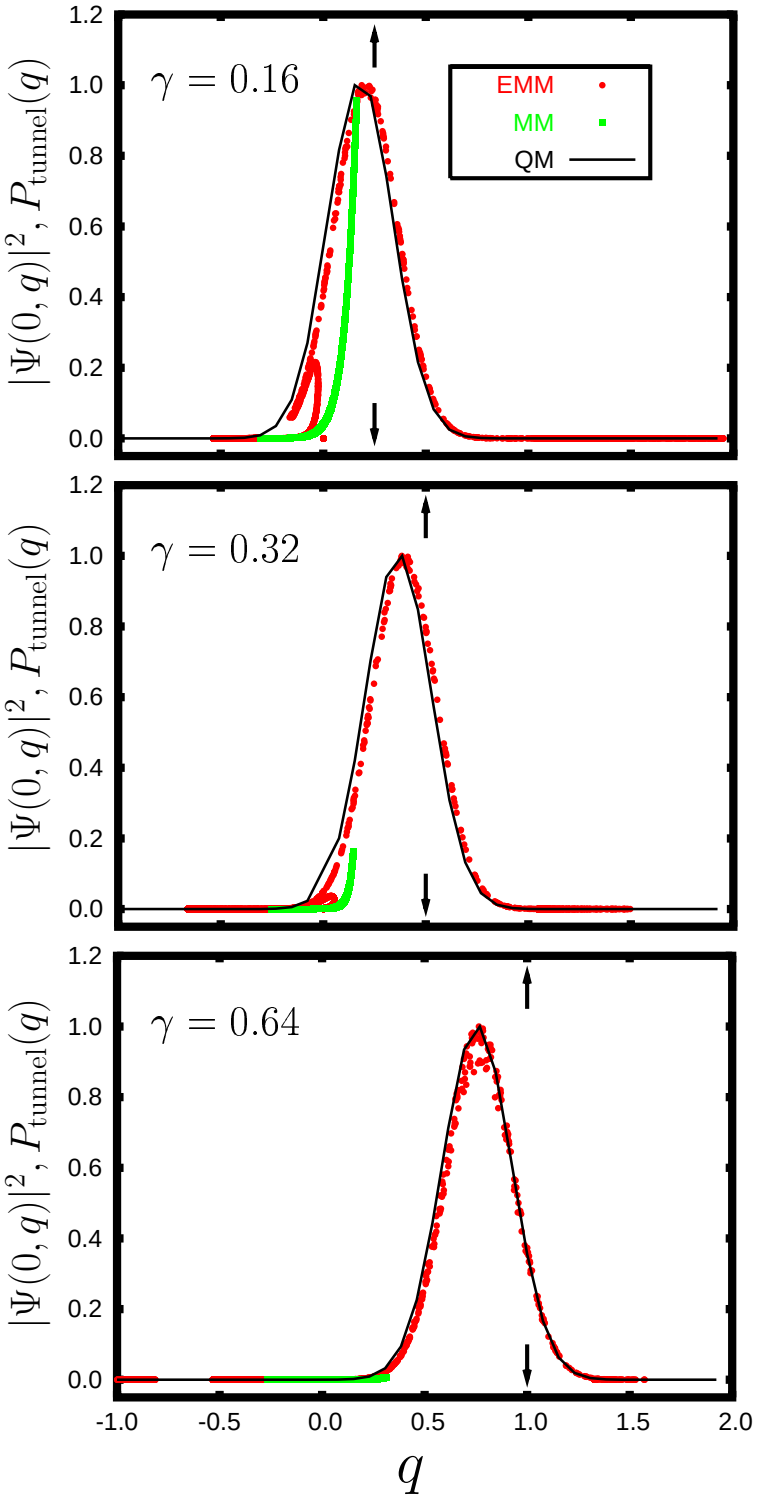

Figure 3.5: SMC Hamiltonian [Eq. (3.17)] with $g = 0.04$, $\omega = 0.8$ and three different values of γ (indicated): The quantum mechanical (QM) density $|\Psi(0,q)|^2$ (dimensionless) along the symmetry line Σ (q dimensionless) is compared with scatter plots of the tunneling probability $P_{\rm tunnel}(q)$ [cf. Eq. (3.21)] computed with, respectively the extended Makri-Miller (EMM) and Makri-Miller (MM) model. The position of the saddle point is indicated by arrows. All curves are normalized (see text). The MM does not account for tunneling through the I-region; this leads to a break-down of the MM for $\gamma = 0.32$ and $\gamma = 0.64$.

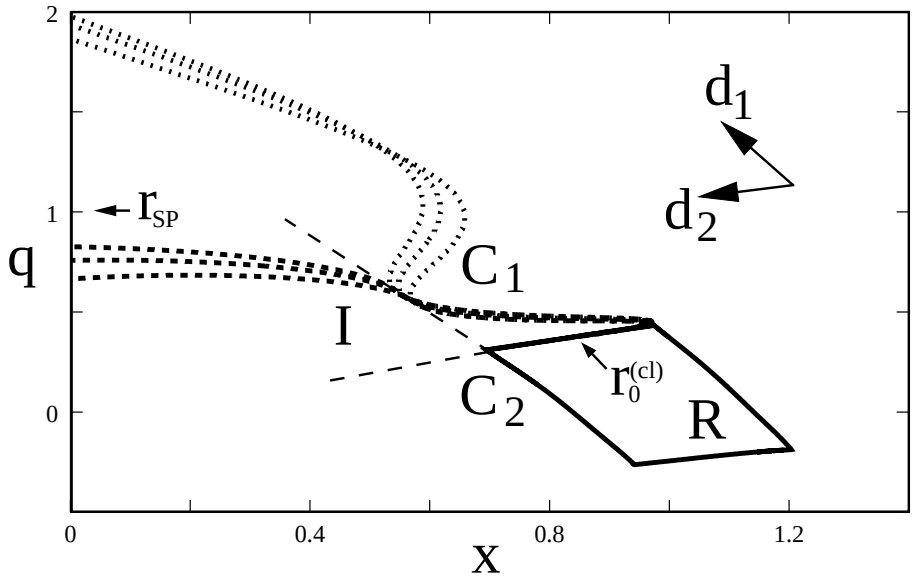

Figure 3.6: SMC Hamiltonian [Eq. (3.17)] with parameters $(\omega, \gamma, g) = (0.64, 0.64, 0.04)$: Trajectories (dimensionless positions) calculated according to the extended Makri-Miller model (EMM). Only the trajectories that propagate through the I-region contribute to the splitting. These trajectories correspond to the maximum of the scatter plot in Fig. 3.5 (lower panel).

the magnitudes of $\exp\{-2\,W_n/\hbar\}$ matter, therefore the magnitude of the MM tunneling splitting agrees with the exact result (cf. Table 3.1).

In the middle panel of Fig. 3.5 ($\gamma = 0.32$) the saddle point is located at $q = 0.5$; the maximum of the QM curve is at $q = 0.38$. The EMM scatter plot agrees with QM result (systematic shift of 0.025) quite well; the second branch at about $q \approx 0$ almost vanishes. Conversely, the MM results show a drastic deviation. Especially, the maximum of the MM is 84% smaller than the EMM maximum. Therefore, this situation indicates the onset of a breakdown of the MM approximation. Upon a further increase of γ the MM scatter values become very small as compared to the EMM values. For instance, this is shown in the lower panel of Fig. 3.5 ($\gamma = 0.64$). Here, the saddle point is at $q = 1.0$ and the QM maximum is at $q = 0.76$, respectively. The EMM scatter plot agrees quite well with the QM results (systematic shift of 0.01). Clearly, in this case only the EMM yields the correct order of magnitude of the tunneling splitting (cf. Table 3.1). Calculated trajectories for the $(0.64, 0.64, 0.04)$ parameter set are shown in Fig. 3.6. Schematically, the same situation was drawn in Fig. 3.2 [case (ii)].

Table 3.2 shows tunneling splitting obtained for the case of small γ (cf. Fig. 3.2a). Values reported as C_2 are obtained for the EMM by taking only that fraction of tunneling trajectories in the sum Eq. (3.13) that tunnel exclusively through

	$\Delta_{(0,0)}$ (ground state)			
(ω, γ)	QM	MM	EMM	C_2
$(0.2, 0.05)$	1.02(-4)	1.03(-4)	1.31(-4)	0.94(-4)
$(0.2, 0.10)$	5.28(-5)	4.89(-5)	6.83(-5)	4.61(-5)
$(0.2, 0.15)$	2.47(-5)	1.76(-5)	2.62(-5)	1.65(-5)
$(0.2, 0.25)$	9.07(-6)	3.48(-6)	8.01(-6)	3.19(-6)
$(0.4, 0.05)$	1.29(-4)	1.38(-4)	1.44(-4)	1.03(-4)
$(0.4, 0.15)$	1.00(-4)	1.15(-4)	1.54(-4)	9.95(-5)
$(0.4, 0.35)$	5.20(-5)	2.53(-5)	6.56(-5)	2.25(-5)

Table 3.2: Same as Tab. 3.1 but for the case of small γ sketched in Fig. 3.2a. The parameter g is 0.08. Splittings reported for C_2 refer to the contribution to the tunneling splitting due to trajectories that tunnel exclusively through the C_2 region.

	$\Delta_{\mathbf{n}}$			
(n_x, n_q)	QM	MM	EMM	C_2
$(0, 0)$	6.63(-9)	1.02(-10)	9.54(-9)	2.34(-11)
$(0, 1)$	2.01(-7)	3.35(-8)	1.77(-7)	2.01(-8)
$(0, 2)$	3.08(-6)	1.35(-6)	2.90(-6)	1.40(-6)
$(0, 3)$	3.16(-5)	2.36(-5)	4.41(-5)	3.28(-5)

Table 3.3: Same as Tab. 3.2 but tunneling splitting of ground and excited states for parameter set $(0.9, 0.7, 0.04)$.

the C_2 region. For the small coupling case both methods, EMM and MM, are reasonable. While the MM typically yields a slight underestimation for the shown parameter sets, the EMM yields overestimations for some parameter sets. The C_2 values are typically very close to the MM results. Thus, the MM underestimation can be attributed to the missing of I-region tunneling [for instance, for $(0.2, 0.25, 0.08)$], but the overestimation is also due to I-region tunneling. However, these deviations are small in view of exponential accuracy.

Finally, the mode-selectivity of the tunneling splitting is addressed. For the symmetric coupling case at hand, the tunneling splitting are supposed to increase by increasing quantum numbers. In Tab. 3.3 this is shown for the parameter set $(0.9, 0.7, 0.04)$. Only excitations of the n_q quantum number are shown. For the ground state $(0, 0)$ the MM yields a tunneling splitting that is almost 2 orders of magnitude too small, while the EMM value is very close to the numerical exact value. For increasing n_q quantum number the underestimation by the MM also

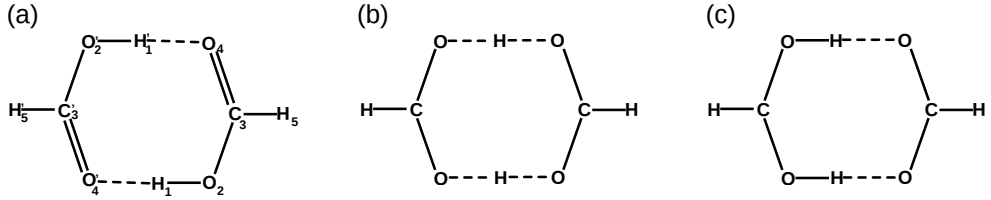

Figure 3.7: Schematic geometries of the formic acid dimer (FAD). (a) minimum (C_{2h}), (b) transition state (D_{2h}), and (c) geometry (C_{2v}) considered in Ref. [117].

decreases. Comparison with the C_2-values unveils that tunneling through the I region is contributing considerably to the tunneling splitting for the ground and first excited state. Thus, the tunneling mechanism changes from I region tunneling to C region tunneling upon excitations. A more detailed study of the application of the EMM to a system with pronounced mode selectivity is studied in Section 3.3.3.

3.3.2 Carboxylic acid dimers

The formic acid dimer (FAD) is the most simple carboxylic acid dimer. The monomers are held together by two hydrogen bonds. The minimum (C_{2h}) and transition state (D_{2h}) geometry of gaseous FAD is shown in Fig. 3.7 [117]. Permutation of corresponding atoms leads from one minimum geometry to an equivalent minimum geometry. The symmetry of the transition state may be changed by polar solvents to have C_{2v} symmetry [117] (cf. Fig. 3.7c). However, the issue seems to depend on the method of quantum chemistry used [117].

FAD was thoroughly investigated by experimental and theoretical techniques. Recently, the ground state tunneling splitting of FAD [more precisely $(DCOOH)_2$] was measured by Madeja and Havenith [12] to be 0.00286 cm^{-1}. Theoretical studies addressed the reaction mechanism. In the gas phase, the structure of FAD was found to keep approximately C_{2h} symmetry along the IRP [118] indicating a concerted transfer as suggested by the transition state geometry. Shida *et al.* [119] investigated a 3D model of FAD; their tunneling splitting value of 0.004 cm^{-1} corresponds rather well with the experimental finding. The barrier height was $49.4\,\mathrm{kJ/mol}$ and the step wise transfer mechanism was found to contribute about 20% to the tunneling splitting. Vener *et al.* [120] obtained a much larger tunneling splitting of $0.3\,\mathrm{cm}^{-1}$ for a similar barrier of $47.7\,\mathrm{kJ/mol}$. For elevated temperatures (or excitation energies) the reaction mechanism may change [121, 122] or not [123]; a clarification considering also the limit $T \to 0$ was not achieved, yet.

For the present purpose a concerted HAT for FAD is assumed, i.e., the tran-

sition state has D_{2h} symmetry. Thus, the PES is of the SMC type (cf. Section 2.2.3). This coupling type is also relevant for, e.g., tropolone and malonaldehyde. (For the step wise HAT two equivalent saddle point geometries do exist and the PES has no longer the SMC shape.) Along the IRP first the monomers approach each other and then the hydrogen transfer takes place [122]. This means, one may vary the IRP curvature by substituting the two hydrogens, H_5 and H_5' by, e.g., fluorines or phenyl rests. In terms of SMC parameters: the coupling strength γ can be varied by choosing different substituents.

A simple method was proposed to determine the necessary SMC parameters [75]. Let $\mathbf{X}_R$ be the $3 \cdot N_{\mathrm{at}}$ dimensional mass-weighted vector corresponding to the geometry of one minimum (denoted as *right*), where $N_{\mathrm{at}} = 10$ is the number of atoms (cf. Section 2.2.1). The center of mass (COM) is at the origin. Likewise, let $\mathbf{X}_L$ and $\mathbf{X}_{TS}$ correspond to the other minimum (denoted as *left*) and the saddle point geometry, respectively. The left ($\mathbf{X}_L$) and right ($\mathbf{X}_R$) minimum is only unique up to an arbitrary rotation. This is removed by rotating $\mathbf{X}_L$ around $\mathbf{X}_R$ in order to minimize the distance $|\mathbf{X}_R - \mathbf{X}_L|$ [75]. Correspondingly, the saddle point geometry $\mathbf{X}_{TS}$ is rotated around the center geometry, $\mathbf{X}_C = (\mathbf{X}_R + \mathbf{X}_L)/2$, in order to minimize $|\mathbf{X}_C - \mathbf{X}_{TS}|$. Then, the two vectors,

$$\mathbf{w}_1 = \frac{\mathbf{X}_R - \mathbf{X}_L}{|\mathbf{X}_R - \mathbf{X}_L|}, \tag{3.22}$$

$$\mathbf{w}_2 = \frac{\mathbf{X}_C - \mathbf{X}_{TS}}{|\mathbf{X}_C - \mathbf{X}_{TS}|}, \tag{3.23}$$

span the so-called *reaction plane*. The reaction plane is also considered in Chapter 5. The vector $\mathbf{w}_1$ corresponds to the direct tunneling direction, i.e., the straight line connecting both minima and the center geometry; the vector $\mathbf{w}_2$ points from the saddle point towards the center geometry. The saddle point of the SMC-PES is at $(0, \alpha)$ where $\alpha = \gamma/\omega^2$ is a ratio of geometry displacements,

$$\alpha \equiv \frac{|\mathbf{X}_C - \mathbf{X}_{TS}|}{|\mathbf{X}_R - \mathbf{X}_C|}. \tag{3.24}$$

The frequency parameter ω is a frequency ratio, $\omega = \tilde{\Omega}_2/\tilde{\Omega}_1$ (cf. Sec. 3.3.1). The frequencies $\tilde{\Omega}_1$ and $\tilde{\Omega}_2$ correspond to $\mathbf{w}_1$ and $\mathbf{w}_2$, respectively, and are determined by weighting the contribution of each normal mode with a component into the $\mathbf{w}_1$ and $\mathbf{w}_2$ direction, respectively,

$$\tilde{\Omega}_k^2 = \sum_j (\boldsymbol{\mathcal{Y}}_j \cdot \mathbf{w}_k)^2 \, \omega_j^2, \quad k = 1, 2, \tag{3.25}$$

where $\boldsymbol{\mathcal{Y}}_j$ with $j = 1, \ldots, N-6$ are the $N = 3 \cdot N_{\mathrm{at}}$ dimensional normal mode vectors of the (right or left) minimum and ω_j are the corresponding normal mode

molecule	FAD	FFAD	BAD[a]
$\Delta E_{\ddagger}$(kJ/mol)	47.6	49.1	40.2
$\Delta E_{\rm zpe}$ (kJ/mol)	1.2	1.5	1.5
$r_{\rm OO}$ (Å)	2.77 (2.44)	2.75 (2.43)	2.69 (2.42)
$r_{\rm OH}$ (Å)	1.00 (1.22)	1.00 (1.21)	1.00 (1.21)
$r_{\rm CC}$ (Å)	3.91 (3.58)	3.80 (3.50)	3.89 (3.63)
$r_{\rm CR}$ (Å)	1.09 (1.09)	1.34 (1.33)	1.49 (1.49)
α[b]	1.28	1.19	1.82
$\omega_{as}/2\pi c\,({\rm cm}^{-1})$	3298	3350	3107
$\omega_m/2\pi c\,({\rm cm}^{-1})$	203 (497)	173 (382)	119 (199)
$\tilde{\Omega}_1/2\pi c\,({\rm cm}^{-1})$	1480	1181	1236
$\tilde{\Omega}_2/2\pi c\,({\rm cm}^{-1})$	471	439	377
SMC parameters (dimensionless)			
$g=\tilde{\Omega}_1/8\Delta E_{\ddagger}$	0.0477	0.0371	0.0477
$\omega=\tilde{\Omega}_2/\tilde{\Omega}_1$	0.318	0.372	0.305
$\gamma=\alpha\,\omega^2$	0.129	0.164	0.169

[a] B3LYP/6-31+G(d) geometry; [b] cf. Eq. (3.24)

Table 3.4: Parameters for carboxylic acid dimers [MP2/6-31+G(d)]: formic acid dimer (FAD), fluoro formic acid dimer (FFAD), and benzoic acid dimer (BAD). The parameters are explained in the text. Parenthesized values correspond to the saddle point geometry. r_{OO} is the $O_2'-O_4$ distance, r_{CC} is the $C_3'-C_3$ distance, r_{CR} is the C_3-H_5 distance, and r_{OH} is the O_2-H_1 distance.

frequencies. The SMC parameter g is given by $g = \tilde{\Omega}_1/8\Delta E_{\ddagger}$ (cf. Section 3.3.1), where $\Delta E_{\ddagger}$ is the zero-point-energy (ZPE) corrected barrier height.

Various parameters of FAD are reported in Table 3.4. All results were obtained in this work by the Gaussian 98 package [124] within the MP2 method using the 6-31+G(d) basis set. Results for a number of different levels of theory and basis sets were also reported in Ref. [118]. Among them, barrier heights $\Delta E_{\ddagger}$ deviate by several $\mathrm{kJ/mol}$ and no rigorous convergence was achieved. The present value, $\Delta E_{\ddagger} = 47.6\,\mathrm{kJ/mol}$, is assumed to be a reasonable estimate at least. However, a very recent high-level quantum chemistry calculation [DFT/aug-cc-pVTZ with CCSD(T) corrections] points towards a lower barrier of $33.1\,\mathrm{kJ/mol}$ [107].

The most prominent geometrical feature is the decrease by 0.33 Å of the r_{OO} and r_{CC} distances (definition: see caption of Tab. 3.4) for the saddle point geometry compared to the minimum geometry. Conversely, the r_{CR} distances do not change, and the two monomers approach each other as a whole. The dimensionless parameter α [cf. Eq. (3.24)] is 1.28. This value is intermediate between tropolone and malonaldehyde with $\alpha = 1.19$ [75] and $\alpha = 1.7$ [74] (in the present notation), respectively.

There are parameters for two derivatives of FAD in Tab. 3.4, too: the fluoro formic acid dimer (FFAD) and the benzoic acid dimer (BAD). In these compounds the two hydrogens, H_5 and H_5' (cf. Fig. 3.7) are substituted by either two fluorine atoms (F) or two phenyl rests (C_6H_5). Both molecules, FFAD and BAD, are planar. The barrier height of FFAD is only slightly increased by 1.5 $\mathrm{kJ/mol}$ as compared to FAD, while for BAD it is 7.4 $\mathrm{kJ/mol}$ lower. (Note, the BAD barrier height was obtained by using the MP2 method together with the B3LYP-DFT optimized geometry.) The variation of the geometrical parameters of the carboxylic ring is moderate among the species. Most prominent is the decreased inter-monomer distance r_{CC} for FFAD (3.80 Å) as compared to FAD (3.91 Å) and BAD (3.89 Å). In all three compounds the monomers move as a whole when approaching the saddle point, which can be deduced from the almost unchanged r_{CR} bond length.

The dimensionless geometrical parameter α for FFAD (1.19) is only slightly smaller than that for FAD (1.28). For BAD (1.82) it is significant larger, because the difference between mass-weighted minimum geometry $\mathbf{X}_R$ and center geometry $\mathbf{X}_C$ is primarily due to the displaced hydrogens, while the difference between saddle point geometry $\mathbf{X}_{TS}$ and $\mathbf{X}_C$ is due to the displacement of the two monomers. Obviously, the monomers are considerably heavier for BAD leading to larger mass-weighted distances than for FAD and FFAD.

The effective frequencies, $\tilde{\Omega}_1$ and $\tilde{\Omega}_2$, were obtained by the projection of normal mode frequencies onto $\mathbf{w}_1$ and $\mathbf{w}_2$, respectively [cf. Eq. (3.25)]. Direction

	ΔE (cm^{-1})				
molecule	QM	MM	EMM	Exp.	GT path
FAD	3.69(-3)	3.20(-3)	5.45(-3)	[a] 2.86(-3)	2.2(-3)
FFAD	3.55(-5)	2.05(-5)	4.55(-5)		5.3(-4)
BAD	1.20(-3)	0.64(-3)	1.41(-3)	[b] 0.22(0)	2.2(-3)

[a] Ref. [12]; [b] Ref. [125] (seleno-indigo doped BAD crystals)

Table 3.5: Tunneling splittings for carboxylic acid dimers (PES parameters and molecule acronyms: see Tab. 3.4) obtained by quantum mechanical (QM), Makri-Miller model (MM), and extended Makri-Miller model (EMM) calculations. Experimental values (Exp.; if available) and values obtained by the approximate method of Tautermann *et al.* [126] based on optimizing Garret-Truhlar (GT) paths (cf. Sec. 3.1.3) are also given.

$\mathbf{w}_2$ corresponds to an effective (i.e., including all modes with a certain overlap) inter-monomer vibration. The frequencies $\tilde{\Omega}_2$ decrease by going from FAD to BAD; this behavior is similar to that of the minimum normal modes of the inter-monomer vibration ω_m and it is mainly a mass effect. The frequencies $\tilde{\Omega}_1$ correspond to direction $\mathbf{w}_1$ which includes mainly the hydrogen motion. The effective frequency $\tilde{\Omega}_1$ of FFAD and BAD is rather different from the parent compound. No such difference can be anticipated from inspecting the anti-symmetric OH stretch frequencies ω_{as}.

The dimensionless SMC parameters are also given in Tab. 3.4 for the three species. The two reactive degrees of freedom are the antisymmetric stretch of the two OH bonds (ω_{as}) and the inter-monomer vibration (ω_m), respectively (for corresponding frequencies cf. Tab. 3.4). The minimum geometry antisymmetric OH stretch turns into the imaginary frequency normal mode at the TS. The two reactive DOF were excluded from the zero-point energy difference ΔE_{zpe}, which is less than $2\,\mathrm{kJ/mol}$ in all cases.

The tunneling splitting ΔE obtained for the three methods QM, MM, and EMM, respectively, is given in Tab. 3.5. For FAD, the numerical exact result ($3.69{\cdot}10^{-3}\,\mathrm{cm}^{-1}$) corresponds well with the experimental value ($2.86{\cdot}10^{-3}\,\mathrm{cm}^{-1}$). In view of the simplicity of the underlying model, this is rather surprising. Probably it indicates, that the effective barrier height is reasonable. The semiclassical methods, MM and EMM, yield the same order of magnitude as the QM. There is a 48% overestimation by the EMM. For the remaining species the findings for comparing MM and EMM are similar. Both methods reproduce the QM values in view of exponential accuracy. The significant deviation of the experimental BAD value

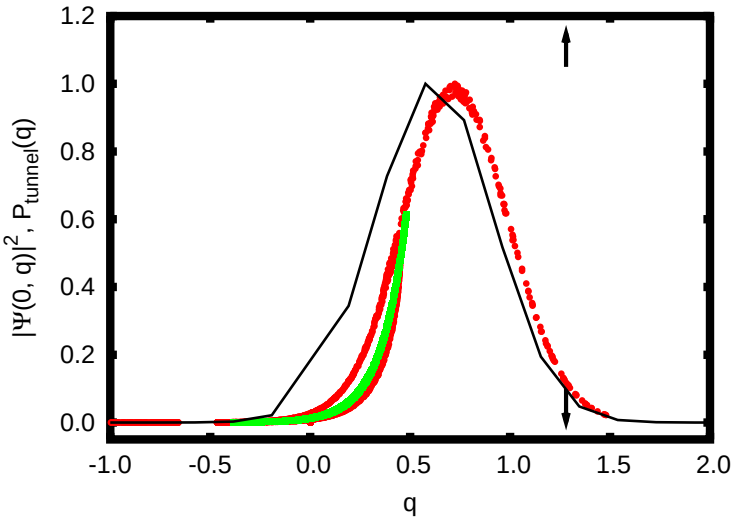

Figure 3.8: Same as Fig. 3.5 but for the SMC parameters $(\omega, \gamma, g) = (0.318, 0.129, 0.0477)$ for the formic acid dimer (FAD). All curves are normalized (see text). The difference between the maximum of the wave function and the saddle point (arrows) indicates pronounced corner cutting. The situation is intermediate between the upper and middle panel of Fig. 3.5 and shows the onset of the break-down of the Makri-Miller model.

from the theoretical predictions was explained by the fact that the experiment was performed for doped crystals of BAD [126].

Recently, Tautermann *et al.* [126] determined tunneling splittings of various carboxylic acid dimers using an approximate version of the instanton method. The values are given in the last column of Tab. 3.5 and marked as "GT path" (cf. also Section 3.1.3). The quantum chemistry was performed by a hybrid approach using a combination of B3LYP/6-31+G(d) and G2(MP2) theory. The barriers for FAD, FFAD, and BAD are, respectively, 37.0, 36.6, and $32.0\ \mathrm{kJ/mol}$. Nevertheless, the values agree with the ones obtained in the present - very simple - model within one order of magnitude; the largest deviation is found for FFAD. The present SMC model and the Garrett-Truhlar (GT) path results predict that the tunneling splitting of FFAD drops signifi cantly as compared to FAD and BAD. (No explanation for this observation was given in Ref. [126].) Concerning the SMC model, inspection of Tab. 3.5 unveils that the reason is the decrease of the projected frequency $\tilde{\Omega}_1$; this leads to smaller g, and larger ω and γ as compared to FAD. The effect is compensated for in BAD by the substantial decrease of $\tilde{\Omega}_2$, which relates to an effective inter-monomer vibration.

The parameters of FAD (and derivatives) do not lead to predominate tunneling through the I region, and the MM yields a reasonable ground state tunneling splitting. Analogous to Fig. 3.5, in Fig. 3.8 the numerical exact density along

	minimum (C_s)	saddle (C_{2v})
R_{HO} (Å)	0.9619	1.1491
R_{OO} (Å)	1.5270	1.6991
γ_{HOO} (deg.)	97.34	42.3

Table 3.6: Geometrical parameters of HO_2^- [129].

the symmetry line, $|\Psi(x=0,q)|^2$, is compared to scatter plots of $\exp\{-2\,W_n/\hbar\}$ vs. q for the two semiclassical methods. The wave function along the symmetry line shows a significant corner cutting: the maximum of the QM density is at about $q = 0.6$ whereas the saddle point is at 1.28. In other words, the tunneling wavefunction tries to prevent movement of the monomers. The EMM maximum is at about $q = 0.7$, i.e., the magnitude of the corner cutting is underestimated by the semiclassical theory. Concerning a comparison between EMM and MM, the situation is intermediate between the upper and middle panel of Fig. 3.5. Thus, tunneling in FAD (and derivatives) is in the turn-over region from C to I region tunneling. The MM tunneling splitting ($3.20 \cdot 10^{-3}\,\mathrm{cm}^{-1}$) is closer to the exact value ($3.69 \cdot 10^{-3}\,\mathrm{cm}^{-1}$) as the EMM result ($5.45 \cdot 10^{-3}\,\mathrm{cm}^{-1}$). The overestimation of the EMM is due to the contribution of the two branches that correspond to trajectories that traverse the $C_1 - I$ and $C_2 - I$ regions, respectively (cf. also Fig. 3.5).

3.3.3 Hydroperoxyl anion HO_2^-

Among the non-rigid triatomics of the form HX_2, the hydroperoxyl anion HO_2^- has a rather low barrier for HAT and the distances of heavy atoms differs considerably for the minimum and saddle point geometry [127]. Therefore, the IRP has a large curvature which is an indication for a truly multidimensional HAT. Chan and Hamilton [127, 128, 129] obtained an accurate PES fit on the QCISD(T)/6-311++G(2df,pd) level of theory. The geometrical parameters are shown in Table 3.6 and the barrier height is $71\,\mathrm{kJ/mol}$ ($5941\,\mathrm{cm}^{-1}$). The 31 lowest vibrational eigenstates were obtained by the same authors. The fundamentals are $3575.1\,\mathrm{cm}^{-1}$ (OH stretch), $1066.7\,\mathrm{cm}^{-1}$ (HOO bend), and $709.8\,\mathrm{cm}^{-1}$ (OO stretch). As expected, the tunneling splittings are considerably mode-specific; for instance, for the OO stretch fundamental the splitting is $2 \cdot 10^{-4}\,\mathrm{cm}^{-1}$ while for a combination excitation with one quantum, respectively, in the OO stretch and HOO bend it is $1 \cdot 10^{-2}\,\mathrm{cm}^{-1}$. Thus, the hydroperoxyl anion is very well suited as a test case for the newly developed EMM, because the tunneling splittings differ by orders of magnitude among different eigenstates.

Both, MM and EMM, are formulated for Cartesian coordinates. For the MM this is because the straight line paths are defined as Cartesian vectors; for the EMM this is because the parities of motion are associated to Cartesian momenta. Guo and Thompson [101] applied the MM to hydrogen peroxide ($HOOH$) and used the torsional angle as tunneling coordinate instead of a straight line. This was possible, because a single internal coordinate was (assumed to be) responsible for the tautomerization. However, a generalization is hardly possible when more internal non-Cartesian coordinates have to be considered. In order to apply MM and EMM to a small molecule like the hydroperoxyl anion, it is therefore necessary to describe the molecule in a Cartesian coordinate system. Two rotational DOF can be removed by confining the motion to a plane. The coordinate vectors $\mathbf{R}$, $\mathbf{r}$, and $\mathbf{s}$ as defined in Fig. 3.9 are employed. The positions of the two oxygen atoms, $\mathbf{r}_1$ and $\mathbf{r}_2$, and the position of the hydrogen atom, $\mathbf{r}_3$, can be expressed as:

$$\mathbf{r}_1 = \mathbf{R} - \mathbf{r}, \tag{3.26}$$

$$\mathbf{r}_2 = \mathbf{R} + \mathbf{r}, \tag{3.27}$$

$$\mathbf{r}_3 = \mathbf{R} + \mathbf{s}. \tag{3.28}$$

Assuming (without restriction) that the center of mass of the triatomic is fixed at the origin, it follows:

$$\mathbf{R} = -\frac{m_H}{M}\mathbf{s}, \tag{3.29}$$

where m_H and M are the mass of a hydrogen and the total mass of the triatomic, respectively. The Lagrangian of the systems reads (cf. Appendix A.3):

$$\mathcal{L} = \frac{1}{2} m_H \left(1 - \frac{m_H}{M}\right) \dot{\mathbf{s}}^2 + \frac{1}{2} \left(2 m_O\right) \dot{\mathbf{r}}^2 - V(\mathbf{s}, \mathbf{r}), \tag{3.30}$$

where m_O is the oxygen mass and $V(\mathbf{s}, \mathbf{r})$ is the PES of the hydroperoxyl anion. The configuration space $(\mathbf{s}, \mathbf{r})$ of this Lagrangian is 4D. This means, because there are three internal coordinates, an individual trajectory is only unique up to an arbitrary rotation around the 4D origin $(\mathbf{s} = \mathbf{0}, \mathbf{r} = \mathbf{0})$. (This corresponds to a rotation around the 6D center of mass.)

The vibrational eigenstates are labeled as $\mathbf{n} = (n_1, n_2, n_3)$, where the quantum numbers correspond to the OH stretch (n_1), HOO bend (n_2), and OO stretch (n_3). The Cartesian description leads to a fourth DOF in Eq. (3.30) that corresponds to rotations in the plane. The corresponding angular momentum is set to zero in the following considerations. The MM and EMM initial conditions for the ensembles of trajectories corresponding to an vibrational eigenstate $\mathbf{n}$ were obtained by normal mode sampling with energy rescaling, where the energy was chosen to be the mean of the exact QM levels. The normal mode analysis with respect to a 4D minimum, $(\mathbf{s}^{(\min)}, \mathbf{r}^{(\min)})$, yields three vibrational normal modes

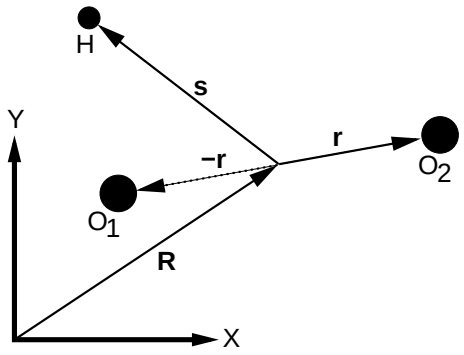

Figure 3.9: Definition of coordinates used for the hydroperoxyl anion.

plus an infinitesimal rotation vector. The normal modes are only guaranteed to be orthogonal to the infinitesimal rotational vector that corresponds to the minimum; for a displaced geometry there is a slightly different rotational vector. Therefore, for each trajectory the angular momentum was removed. In order to fix the energy, the momenta were scaled. This is similar to the usual procedure of energy rescaling (cf. Section 2.1.5). The trajectories were integrated by a fifth-order symplectical integrator [116] with a fixed step-size of $0.48\,\mathrm{fs}$. The energy was bound within a typical maximum tolerance of $0.1\,\mathrm{cm}^{-1}$.

Power spectra (cf. Section 2.1.5) for ensembles of 100 classical trajectories for, respectively, the ground state $(0,0,0)$ at total energy $2676\,\mathrm{cm}^{-1}$ and state $(0,1,5)$ at total energy $7000\,\mathrm{cm}^{-1}$ are shown in Fig. 3.10. The state $(0,1,5)$ was chosen as a typical example for a highly excited state. In both spectra one may identify three main peaks that correspond to quasiperiodic motion with the three fundamental frequencies. For the ground state spectrum these peaks are narrow. This indicates, that phase space points on (or very close to a) certain invariant torus are sampled. Comparison with the exact QM fundamentals (dashed vertical lines) shows, that this certain invariant torus almost coincides with the ground state invariant torus. Conversely, in the spectrum of state $(0,1,5)$ the main peaks are broadened and posses a substructure. The significant shifts of the peak maxima with respect to the QM fundamentals are due to the anharmonicity of the potential. Thus, for the state $(0,1,5)$ one expects the normal mode sampling to be less efficient. Nevertheless, the appearance of three main peaks indicates, that an invariant torus corresponding to the QM state exists at least approximatively.

For the MM the tunneling direction is defined such, that the OO distance vector $2\mathbf{r}$ is held fixed for the tunneling process, i.e., at each point $(\mathbf{s},\mathbf{r})$ the tunneling direction is preliminary given by:

$$\mathbf{d}'_{\mathrm{MM}} = \begin{pmatrix} \mathbf{r}/|\mathbf{r}| \\ \mathbf{0} \end{pmatrix}. \tag{3.31}$$

The choice was also used for malonaldehyde in Refs. [100, 103]. If the hydrogen

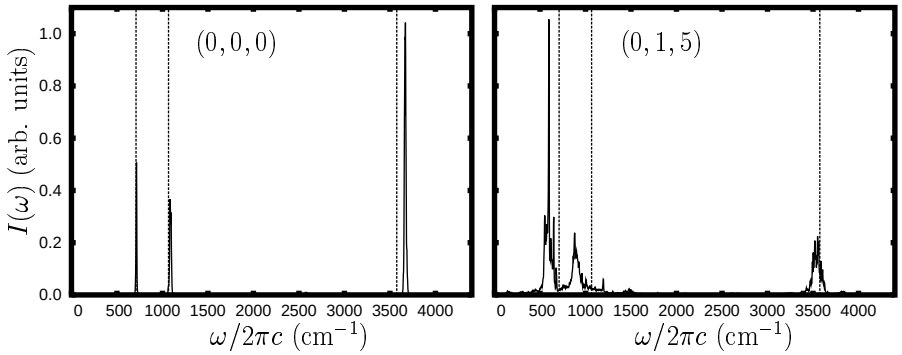

Figure 3.10: Results for the HO_2^- model Lagrangian [Eq. (3.30)] with the PES of Chan and Hamilton [128, 129]: Power spectra $I(\omega)$ [cf. Eq. (2.40)] for the ground state $(0,0,0)$ and excited state $(0,1,5)$, respectively. The power spectra were obtained by propagating ensembles of 100 trajectories and Fourier transformation of $Z(t) = \sum_i P_i(t)$ with Gaussian broadening $\exp\{-t^2/\tau^2\}$ and τ = 5 ps. The propagation time was 14.5 ps. Fundamentals are indicated as dashed lines.

is located in the left well (i.e., $\mathbf{s} \cdot \mathbf{r} < 0$) then a straight line along $\mathbf{d}'_{\mathrm{MM}}$ leads automatically to a C_{2v} confi guration of the triatomic. This confi guration is a point on the symmetry surface Σ that is defi ned by $\mathbf{s} \cdot \mathbf{r} = 0$.

Clearly, the molecule rotates along a straight line defi ned by Cartesian directions as given by Eq. (3.31). This is, because only the hydrogen moves along these straight lines and the complementary counter-rotation of the OO axis is missing. Due to the mass ratio of about 1:16 between hydrogen and oxygen the error introduce by the straight line approximation may be small. However, the magnitude of this error is unknown a-priori.

The *rotational error* may be reduced by considering a modifi ed tunneling direction that is given by:

$$\mathbf{d}_{\mathrm{MM}} = \frac{\mathbf{d}'_{\mathrm{MM}} - (\mathbf{d}'_{\mathrm{MM}} \cdot \boldsymbol{\rho})\,\boldsymbol{\rho}}{|\mathbf{d}'_{\mathrm{MM}} - (\mathbf{d}'_{\mathrm{MM}} \cdot \boldsymbol{\rho})\,\boldsymbol{\rho}|}, \tag{3.32}$$

where $\boldsymbol{\rho} = \boldsymbol{\rho}(\mathbf{s}_1, \mathbf{r}_1)$ is the infi nitesimal rotational vector at the (turning) point $(\mathbf{s}_1, \mathbf{r}_1)$. With defi nition Eq. (3.32) the rotation in the vicinity of the turning point is removed. A complete rotation free path may be obtained by solving the ordinary differential equation:

$$\frac{d\mathbf{X}}{d\xi} = \mathbf{d}_{\mathrm{MM}}[\mathbf{X}(\xi)], \tag{3.33}$$

where $\mathbf{X}(\xi)$ is a 4D vector as a function of the coordinate ξ along the curved path. The tunneling direction Eq. (3.32) is considered to be $\mathbf{X}$ dependent, such that $\boldsymbol{\rho}$ is evaluated at each point on the path while $\mathbf{d}'_{\mathrm{MM}}$ is held fi xed.

In the present study the MM tunneling integral [Eq. (3.5)] was computed in two ways: (i) by following a straight line tunneling path defi ned by the direction

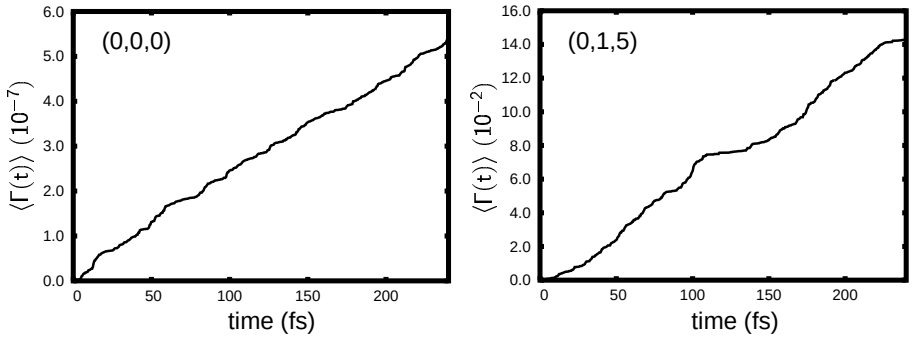

Figure 3.11: Results for the HO_2^- model Lagrangian [Eq. (3.30)] with the PES of Chan and Hamilton [128, 129]: Cumulated extended Makri-Miller model (EMM) tunneling probabilities $\langle\Gamma(t)\rangle$ [Eq. (3.13)] for the ground state $(0,0,0)$ and excited state $(0,1,5)$, respectively (ensemble of 1000 trajectories).

Eq. (3.32) and (ii) by following the curved and rotation free path as defined by the ODE (3.33). In both cases turning points are given by the zeros of $\mathbf{P}\cdot\mathbf{d}_{\mathrm{MM}}$, where $\mathbf{P}$ is the 4D momentum. For the ODE this defines the initial condition for the path, too.

In analogy to Eq. (3.32) the EMM turning point condition [cf. Eq. (3.12)] was modified, such that for each point $(\mathbf{s},\mathbf{r})$ the set of vectors $\{\boldsymbol{\rho},\mathbf{d}_1',\mathbf{d}_2',\mathbf{d}_3'\}$ is Schmidt orthogonalized. Here, $\mathbf{d}_i'$ correspond to the normal mode direction of the three fundamental vibrations at the minimum. The procedure guarantees, that for a turning point $\mathbf{P}\cdot\mathbf{d}_i=0$ with Schmidt-orthogonalized normal mode vector $\mathbf{d}_i$, the parity of motion is flipped to -1 for a direction that is orthogonal to the rotational direction at the turning point. The generalized trajectories are then generated for a reduced space, that is spanned by the three Schmidt-orthogonalized normal mode directions $\mathbf{d}_i$. Therefore, this is a generalization of the condition used for the MM tunneling directions and turning points. Especially, the straight line generated by direction Eq. (3.32) can be expressed as a linear combination of the $\mathbf{d}_i$. The integration of a generalized trajectory is stopped, when the symmetry line Σ has been reached, i.e., when $\mathbf{s}\cdot\mathbf{r}\geq 0$.

For each vibrational level $\mathbf{n}$ ensembles of 1000 classical trajectories were propagated (see above). The fixed step-size was $0.48\,\mathrm{fs}$; for the accurate determination of turning points the step size was reduced to $0.048\,\mathrm{fs}$. The propagation time was $240\,\mathrm{fs}$ which corresponds to about 5 times the vibrational period of the weakest mode. In Fig. 3.11 cumulated EMM tunneling probabilities $\langle\Gamma(t)\rangle$ for, respectively, the ground state $(0,0,0)$ and state $(0,1,5)$ are shown. Corresponding power spectra were shown in Fig. 3.10. Compared to the ground state $\langle\Gamma(t)\rangle$ there is an oscillation superimposed on the approximate linear increase of $\langle\Gamma(t)\rangle$ for state $(0,1,5)$. This can be attributed to the sampling method, i.e., the trajec-

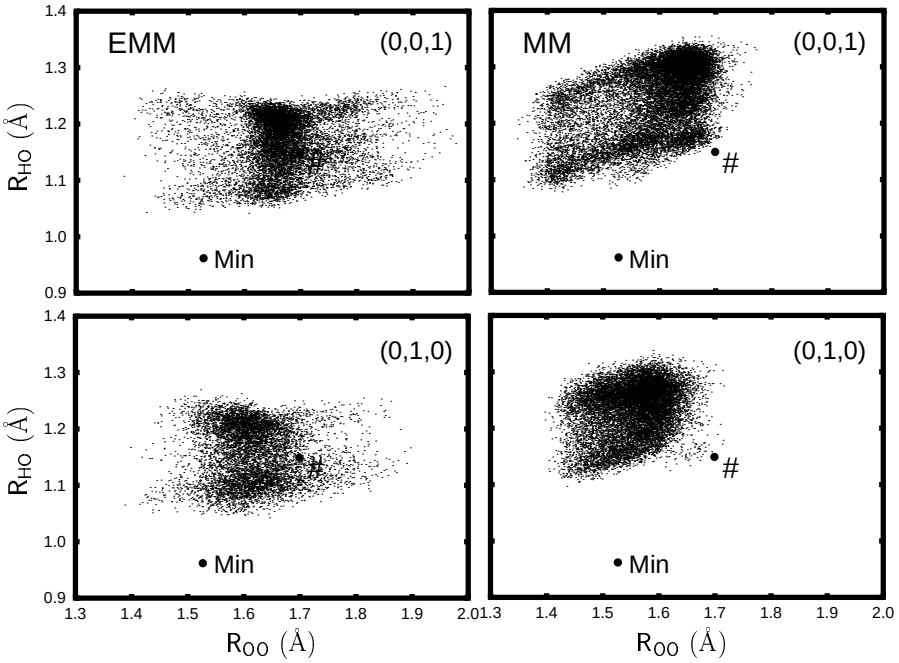

Figure 3.12: Results for the HO_2^- model Lagrangian [Eq. (3.30)] with the PES of Chan and Hamilton [128, 129]: Point cloud plot of the tunneling probability at the symmetry surface (C_{2v} configuration) for two vibrational eigenstates (indicated) obtained by the Makri-Miller model (MM) and the extended Makri-Miller model (EMM). The local density of points at (R_{HO}, R_{OO}) is proportional to $\langle \sum_n (W_n)^{-4} \rangle$, where W_n is the action obtained for a path from the n-th turning point to the point (R_{HO}, R_{OO}) on the symmetry surface. The saddle point ("‡") is indicated; the minimum is not a point on the symmetry surface, but the minimum bond length values (cf. Tab. 3.6) are given for comparison and marked by "Min".

tories are only near the invariant torus [99]. Only those states are considered, for which the linear regression of the data points yields a relative standard deviation of less than 1 %; in particular, this leads to an exclusion of the states with $n_1 = 1$. The sampling error of the tunneling splitting was estimated by performing five distinct runs for the $(0, 0, 1)$ level; the relative standard deviation was 8 %.

In Table 3.7 mode-specific tunneling splittings obtained by diagonalizing the Hamiltonian (QM; taken from Ref. [128]) are compared with semiclassical results obtained within, respectively, the MM and EMM. For the MM results obtained for the two definitions of tunneling paths (discussed above) are also given. The differences of these MM results is negligible. Thus, the rotational error may be neglected. Comparing the MM results for, e.g., the fundamental of the OO vibration $(0, 0, 1)$ with the QM, one finds an underestimation of almost one order of magnitude. Conversely, the EMM result for that vibrational state corresponds quite well to the QM result. The same finding applies to overtones of the OO vibration

	$E^{\pm}_{\mathbf{n}}/hc\ (cm^{-1})$		$\Delta_{\mathbf{n}}/hc\ (cm^{-1})$			
state	+	-	QM	MM[a]	MM[b]	EMM
(0,0,0)	0.0	0.0	—	0.00003	0.00003	0.00002
(0,0,1)	709.8	709.8	0.0002	0.00004	0.00004	0.0003
(0,1,0)	1066.7	1066.7	0.0009	0.001	0.001	0.004
(0,0,2)	1408.7	1408.7	0.001	0.0001	0.0001	0.002
(0,1,1)	1753.4	1753.4	0.01	0.01	0.01	0.03
(0,2,0)	2084.3	2084.3	0.03	0.1	0.1	0.2
(0,0,3)	2092.5	2092.5	0.004	0.0007	0.0008	0.007
(0,1,2)	2426.2	2426.3	0.08	0.1	0.1	0.1
(0,2,1)	2745.3	2745.6	0.3	1.2	1.2	1.1
(0,0,4)	2756.8	2756.8	0.02	0.005	0.005	0.03
(0,3,0)	3063.5	3064.1	0.6	3.4		2.8
(0,1,3)	3081.2	3081.5	0.3	0.9		0.7
(0,2,2)	3388.2	3390.2	2.0	7.1		5.6
(0,0,5)	3398.9	3399.1	0.2	0.06		0.2
(0,3,1)	3692.5	3698.3	5.8	10.3		9.9
(0,1,4)	3714.9	3716.1	1.2	3.9		3.2
(0,4,0)	4000.4	4011.0	10.6	14.2		13.5
(0,2,3)	4010.6	4013.5	2.9	10.4		9.2
(0,0,6)	4017.1	4020.0	2.9	0.3		0.6
(0,3,2)	4285.0	4316.4	31.4	10.1		9.5
(0,1,5)	4323.9	4328.1	4.3	8.9		6.7
(0,4,1)	4562.1	4606.9	44.8	9.9		9.2
(0,2,4)	4600.0	4620.9	20.9	10.8		8.6
(0,0,7)	4608.3	4624.3	16.0	1.6		2.4
(0,5,0)	4826.9	4916.3	89.4	7.7		7.4
(0,3,3)	4895.2	4919.6	24.4	6.1		5.0
(0,1,6)	4907.2	4931.4	24.2	9.5		8.9

[a] straight lines with direction given by Eq. (3.32)

[b] rotation free path given by Eq. (3.33)

Table 3.7: Mode specific tunneling splittings ΔE obtained for the HO_2^- model Lagrangian [Eq. (3.30)] with the PES of Chan and Hamilton [128, 129]. Quantum mechanical (QM) results from Ref. [128] (energies $E^{\pm}_{\mathbf{n}}$ and splittings) are compared with results calculated by the Makri-Miller model (MM) with two different definitions of the tunneling direction (see text) and results calculated by the extended Makri-Miller model (EMM).

up to state $(0,0,5)$. For the fundamental of the OH bend vibration, $(0,1,0)$, the tunneling splittings is overestimated by the EMM. The same applies for the states $(0,2,0)$ and $(0,3,0)$. Also the MM yields overestimated tunneling splittings for the two states $(0,2,0)$ and $(0,3,0)$.

In Fig. 3.12 the magnitude of the tunneling action W_n at the symmetry surface Σ is visualized for the two states $(0,0,1)$ and $(0,1,0)$ by point-cloud plots for the EMM and MM, respectively. The local density of points is proportional to $\sum_n W_n^{-4}(\mathbf{r})$, where $\mathbf{r}$ is a point on the symmetry surface: higher density corresponds to smaller action and, thus, larger tunneling probability. For state $(0,0,1)$ the maximum of the EMM and MM is at $(R_{\mathrm{HO}}, R_{\mathrm{OO}}) \approx (1.2, 1.65)$ and $(1.3, 1.65)$, respectively. Thus, the EMM prefers tunneling at shorter R_{HO} values that are closer to the transition state. This is clearly the reason for the larger tunneling probabilities leading in turn to a larger tunneling splitting. For state $(0,1,0)$ the finding is qualitatively equivalent, but the shift is less pronounced. In this case, however, the effect contributes to the overestimation. Overestimation by the EMM were also found in Section 3.3.1 and 3.3.2. However, it was shown for the generic PES that the EMM in all cases yields a reasonable order of magintude for the splitting, while the MM may break down. It is shown below, that a similar conclusion can be drawn for the present HO_2^- molecule concerning different states.

In order to visualize the performance of the EMM as compared to the MM more globally, the semiclassical results are plotted vs. the QM results in Fig. 3.13 on a double logarithmic scale. The EMM results do systematically overestimate the QM results for splittings smaller than about $2\ \mathrm{cm}^{-1}$ ($log_{10}2 \approx 0.3$). The MM results deviate typically much stronger from the QM values than the EMM results. The log-values for all splittings $\leq 2\,\mathrm{cm}^{-1}$ were fitted by a linear function, $f(x) = A + B \cdot x$ with $x = \Delta(QM)$. For the MM and EMM it was found $(A, B) = (0.5 \pm 0.2, 1.3 \pm 0.1)$ and $(0.4 \pm 0.1, 1.04 \pm 0.05)$, respectively. For an exact correlation one would expect $(0,1)$. Thus, the difference between the EMM and QM results is mainly the constant factor $10^{0.4} \approx 2.5$. In particular, a *calibration* of the results would be reasonable if certain exact splittings are known. The correlation of the MM tunneling splittings with the QM splittings appears to be more erratic. There is a significant deviation from slope 1 and the results can not be corrected by simply introducing a constant factor. For states with splittings larger than about $2\,\mathrm{cm}^{-1}$ there are also underestimations by the EMM. These states are rather highly excited, i.e., the normal mode sampling is less efficient which is most likely a major source of error. Moreover, the quantum spectrum is dominated by a 2:3 Fermi resonance between the OH bend and the OO vibration [127]. This leads to a perturbation of the spectra that cannot be

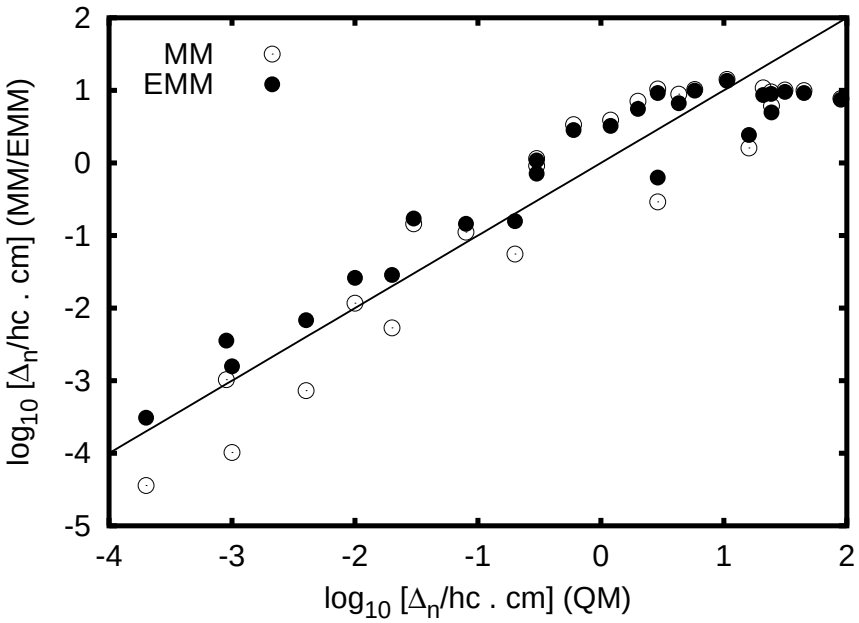

Figure 3.13: Results for the HO_2^- model Lagrangian [Eq. (3.30)] with the PES of Chan and Hamilton [128, 129]: Mode-specific tunneling splittings Δ_n (logarithmic). Values (cf. Tab. 3.7) obtained by MM and EMM vs. exact QM result. The solid line corresponds to perfect agreement. Stronger deviations for larger splittings are due to less accurate trajectory sampling for elevated energies and Fermi resonances (see text).

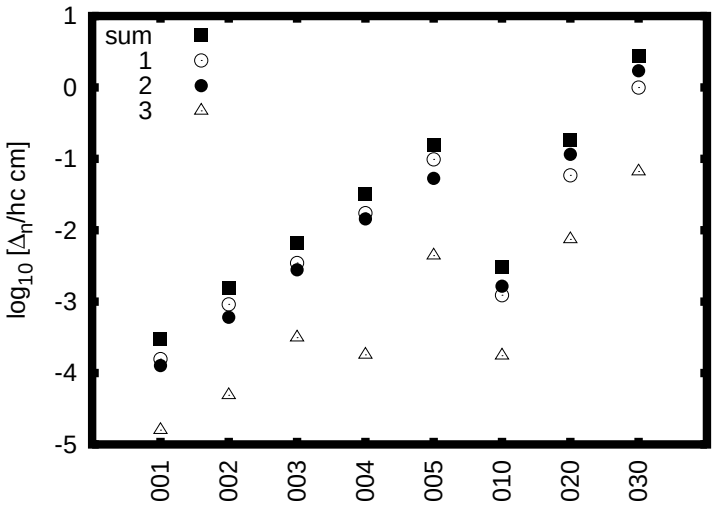

Figure 3.14: Results for the HO_2^- model Lagrangian [Eq. (3.30)] with the PES of Chan and Hamilton [128, 129]: Mode-specific tunneling splittings Δ_n (logarithmic) obtained by the EMM: values for tunneling with one ("1"), two ("2"), and ("3") negative parities, and the sum ("sum") [cf. Tab. 3.7] are shown.

accounted for by the present semiclassical methods.

Finally, the results are analyzed with respect to the number of parities that were flipped. Fig. 3.14 shows EMM tunneling splittings for selected fundamentals and overtones [cf. Tab. 3.7] and tunneling splittings that were obtained by keeping only those W_n in the sum Eq. (3.13) for which there were, respectively, one ("1"), two ("2"), or three ("3") negative parities when the TU trajectory crossed the symmetry line; the sum ("sum") corresponds to the values given in Tab. 3.7. The case of three negative parities is irrelevant. Surprisingly, both cases with one and two parities contribute by almost equal amounts (in a logarithmic sense). For the SMC PES (cf. Section 3.3.1) the Makri Miller tunneling direction $\mathbf{d} = (-1, 0)^t$ becomes equivalent to one of the normal modes for $\gamma \to 0$. For the hydroperoxyl anion, however, the normal modes do not coincide with the definition of the straight line direction [Eq. (3.32]. Thus, the reason for the better performance of the EMM for the hydroperoxyl anion can be attributed to the more physical (still, however, crude) treatment of the connection condition of the semiclassical wave function across the R, C, and I regions.

3.3.4 Conclusion

An extension [I] of the Makri-Miller model [29] was introduced, where tunnel processes are described by means of trajectories that are propagated in the forbidden region (i.e., "under the barrier"). The equations of motion of theses tra-

jectories were given by Takatsuka and Ushiyama (TU theory; cf. Section 2.1.4) [27, 60, 28, 61, 62]. A turning point condition [Eq. (3.12)] based on normal modes was introduced and shown to be reasonable for the present applications. In order to scrutinize the the extended Makri-Miller model (EMM) it is necessary to compare with quantum mechanical exact results. To this end, applications to systems with two and three dimensions were shown for which exact results are present.

The numerical investigation of generic SMC-PES [cf. Eq. (3.17)] showed that for increasing coupling γ straight-line tunneling paths may underestimate tunneling probabilities by orders of magnitude. TU trajectories propagated on the $(-1,-1)$ sheet were shown to be necessary in such cases. For SMC fits to carboxylic acid dimers it was found, however, that both, MM and EMM, yield reasonable results, because corner cutting is very pronounced for these molecules.

The EMM was also applied to an ab-initio PES of the HO_2^- anion [127]. For moderate excitation energies the EMM performs systematically better than the MM for the description of tunneling in this molecule. In particular, a calibration in order to correct the tunneling prefactor seems reasonable (but was not attempted here). Tunneling with one and two parities was found to be almost equally important (in a logarithmic sense). Concerning this molecule, the main advantage of the EMM is the more physical description of the connection of the semiclassical wave function across the different regions.

Ben-Nun and Martínez [103] implemented the Makri-Miller model into ab-initio molecular dynamics simulations with on-the-fly calculation of the PES. This would also be possible for the present EMM. However, the numerical complexity is increased. First, significantly more tunneling trajectories are calculated and several of them are discarded. Second, the solution of Hamilton's equation of motion for the TU trajectories will typically require a smaller step size than the calculation of the PES along a straight line.